

Two Planets Straddling the Habitable Zone of The Nearby K dwarf Gl 414A

CAYLA M. DEDRICK,^{1,2} BENJAMIN J. FULTON,^{1,3} HEATHER A. KNUTSON,¹ ANDREW W. HOWARD,¹ THOMAS G. BEATTY,⁴ PHILLIP A. CARGILE,⁵ B. SCOTT GAUDI,⁶ LEA A. HIRSCH,⁷ RUDOLF B. KUHN,^{8,9} MICHAEL B. LUND,³ DAVID J. JAMES,^{5,10} MOLLY R. KOSIAREK,^{11,*} JOSHUA PEPPER,¹² ERIK A. PETIGURA,¹³ JOSEPH E. RODRIGUEZ,⁵ KEIVAN G. STASSUN,^{14,15} AND DANIEL J. STEVENS^{2,16,†}

¹ California Institute of Technology, Pasadena, CA 91125, USA

² Department of Astronomy & Astrophysics, The Pennsylvania State University, University Park, PA 16802, USA

³ IPAC-NASA Exoplanet Science Institute, Pasadena, CA 91125, USA

⁴ Department of Astronomy and Steward Observatory, University of Arizona, Tucson, AZ 85721

⁵ Center for Astrophysics | Harvard & Smithsonian, 60 Garden Street, Cambridge, MA 02138, USA

⁶ Department of Astronomy, The Ohio State University, 140. W. 18th Ave., Columbus, OH 43210, USA

⁷ Kavli Institute for Particle Astrophysics and Cosmology, Stanford University, Stanford, CA 94305, USA

⁸ South African Astronomical Observatory, PO Box 9, Observatory, 7935, Cape Town, South Africa

⁹ Southern African Large Telescope, PO Box 9, Observatory, 7935, Cape Town, South Africa

¹⁰ Black Hole Initiative at Harvard University, 20 Garden Street, Cambridge, MA 02138, USA

¹¹ Department of Astronomy and Astrophysics, University of California, Santa Cruz, CA 95064, USA

¹² Department of Physics, Lehigh University, 16 Memorial Drive East, Bethlehem, PA, 18015, USA

¹³ Department of Physics and Astronomy, University of California, Los Angeles, CA 90095, USA

¹⁴ Vanderbilt University, Department of Physics & Astronomy, 6301 Stevenson Center Ln., Nashville, TN 37235, USA

¹⁵ Fisk University, Department of Physics, 1000 18th Ave. N., Nashville, TN 37208, USA

¹⁶ Center for Exoplanets and Habitable Worlds, The Pennsylvania State University, 525 Davey Lab, University Park, PA 16802, USA

ABSTRACT

We present the discovery of two planets orbiting the nearby (D=11.9 pc) K7 dwarf Gl 414A. Gl 414A b is a sub-Neptune mass planet with $M_b \sin i_b = 9.28_{-2.54}^{+3.19} M_{\oplus}$ and a semi-major axis of 0.24 ± 0.01 au. Gl 414A c is a sub-Saturn mass planet with $M_c \sin i_c = 59.48_{-9.69}^{+9.98} M_{\oplus}$ and a semi-major axis of 1.43 ± 0.06 au. We jointly analyzed radial velocity data from Keck/HIRES and the Automated Planet Finder at Lick Observatory, as well as photometric data from KELT, to detect the two planets as well as two additional signals related to the rotationally-modulated activity and the long term magnetic activity cycle of the star. The outer planet in this system is a potential candidate for future direct imaging missions.

1. INTRODUCTION

High precision radial velocity (RV) instruments have improved in performance in recent years as the community moves toward the \sim cm s⁻¹ precision range. When combined with high cadence observational campaigns, these measurements make it possible to discover new low mass planets around nearby stars. Statistical methods have also improved greatly, with techniques like Gaussian processes (GPs) to model activity signals (e.g., Dai et al. 2017) making it easier to differentiate between exoplanetary and low-level activity-related signals (Bastien et al. 2013). The use of a GP ensures that our posteriors for the orbital parameters of the two planets properly account for the RV variations caused by rotationally-

modulated star spots and other sources of stellar activity.

The Eta-Earth Survey utilized the W. M. Keck Observatory and the HIRES instrument (Vogt et al. 1994) to search 230 of the nearest G, K, and M dwarf stars for low mass (3-30 M_{\oplus}) planets (Howard et al. 2009). This survey unveiled the mass-distribution of small planets and demonstrated that the occurrence rate of planets is a strong inverse function of their mass (Howard et al. 2010). Our group continues to measure RVs for all of the Eta-Earth stars at reduced cadence with both Keck-HIRES and the Automated Planet Finder telescope (APF, Vogt et al. 2014). Some of these stars have been observed for more than two decades, providing sensitivity to planets with orbital periods of many years. At the same time, recent high cadence observing campaigns with the APF have been very important in detecting

* NSF Graduate Research Fellow

† Eberly Research Fellow

lower mass planets and disentangling planetary signals from stellar activity (Fulton et al. 2016; Fulton 2017).

The Eta-Earth Survey stars are an ideal test set for utilizing Gaussian processes to model stellar activity in exoplanet detection because of the multi-decadal baseline and large number of measurements. We continue to observe stars from the Eta-Earth survey in hopes of finding more small planets with longer orbital periods. Exoplanets with orbital periods greater than 700 days make up less than 10% of the confirmed planet sample (311 out of 4201)¹. Due to sensitivity constraints, a majority of these long-period planets are gas giants.

In this paper, we report the discovery of two planets orbiting the nearby K dwarf Gl 414A. This star shows RV variations caused by stellar activity with amplitudes comparable to the planetary signals, which makes it a perfect candidate for combining RV and photometry data in order to differentiate between the types of signals. In Section 2, we provide an updated analysis of the properties of the host star. We describe our Doppler measurements from Keck/HIRES and APF/Levy in Section 3, and describe our photometry measurements from KELT in Section 4. In Section 5 we describe our joint analysis of the RV data and photometric data. This includes a Keplerian analysis of significant periodic signals in the RVs and a characterization using GPs to model stellar activity. Section 6 discusses the orbital dynamics, transit and direct imaging prospects. We summarize and conclude in Section 7.

2. STELLAR PROPERTIES

Gl 414A, also known as HD 97101A and HIP 54646A, is a bright nearby K7V dwarf star (Gray et al. 2003) at a distance of 11.89 ± 0.07 pc (Gaia Collaboration et al. 2018, Gaia18 here-after). Gl 414A has an M2V dwarf companion (Stephenson 1986) with a V-band magnitude of 9.98 (Zacharias et al. 2012). The projected on-sky separation between Gl 414A and Gl 414B is 34.34 arcsec (Mason et al. 2001), corresponding to a projected physical separation of 408 AU. The stars are widely enough separated that spectral contamination from Gl 414B is not a concern.

2.1. *SpecMatch-Emp* & *isoclassify*

We inferred stellar properties using the publicly available software package **SpecMatch-Emp** (Yee et al. 2017) to quantitatively compare our iodine-free template spectrum of Gl 414A to a suite of library HIRES spectra for stars with well-measured parameters. The

SpecMatch-Emp analysis returned $T_{\text{eff}} = 4120 \pm 70$ K, $[\text{Fe}/\text{H}] = 0.24 \pm 0.09$, and $R_{\star} = 0.680 \pm 0.10 R_{\odot}$.

Since **SpecMatch-Emp** does not return a stellar mass, we used the **isoclassify** package (Berger et al. 2020; Huber et al. 2017) to place the star onto MESA Isochrones & Stellar Tracks (Dotter 2016; Choi et al. 2016a, MIST) isochrone tracks. We followed the methodology of Fulton & Petigura (2018) to derive physical stellar parameters from the spectroscopic parameters. We ran **isoclassify** in both “direct” mode and “grid” mode. In direct mode **isoclassify** relies on a single apparent magnitude (m_K in this case), the extinction in that band, the distance modulus, and a bolometric correction obtained by interpolating the MIST/C3K model grid (Conroy et al., in prep). In grid mode, the star is compared to the isochrones using observational constraints. We informed the **isoclassify** fit by placing priors on Teff and [Fe/H] from our spectroscopic analysis, the Gaia parallax ($\pi = 84.08 \pm 0.471$ mas, Gaia Collaboration et al. (2018)), and the K-band apparent magnitude ($m_K = 4.979 \pm 0.018$ mag, Cutri et al. (2003)). **isoclassify** then calculated the posterior probability density for R_{\star} using the Stefan-Boltzmann law. In direct mode, we found that $L_{\star} = 0.119 \pm 0.005 L_{\odot}$ and $R_{\star} = 0.679 \pm 0.027 R_{\odot}$. Running **isoclassify** in grid mode also allowed us to extract $M_{\star} = 0.650 \pm 0.028 M_{\odot}$ and age = 11.2 ± 5.9 Gyr.

We carried out the same analysis to determine stellar properties of the companion, Gl 414B. **SpecMatch-Emp** returned $T_{\text{eff}} = 3663 \pm 70$ K, $[\text{Fe}/\text{H}] = 0.08 \pm 0.09$, and $R_{\star} = 0.515 \pm 0.100 R_{\odot}$. Because Gl 414B is sufficiently cool, **isoclassify** is able to determine masses in direct mode using empirical relations from (Mann et al. 2019). We found that $R_{\star} = 0.548 \pm 0.017 R_{\odot}$, $M_{\star} = 0.542 \pm 0.022 M_{\odot}$, and $L_{\star} = 0.048 \pm 0.005 L_{\odot}$. In grid mode, we derive age = 12.4 ± 5.2 Gyr.

If the two stars formed in the same birth cloud, we would expect the value of [Fe/H] and the ages of the two stars to be the same, and indeed the values we derive from **SpecMatch-Emp** and **isoclassify** analysis are consistent to 1σ .

We adopt the values of T_{eff} and [Fe/H] from **SpecMatch-Emp**, and the values of R_{\star} , M_{\star} , L_{\star} , and age from **isoclassify**. See Table 1 for the final adopted stellar parameters for both stellar components in the system.

2.2. *MINESweeper*

We also determine stellar parameters using **MINESweeper**, a tool to model stellar photometry using isochrone priors. Full details and validation of this technique can be found in Cargile et al. (2019), but briefly,

¹ <https://exoplanetarchive.ipac.caltech.edu/>

the program can fit broadband photometric stellar spectral energy distributions (SEDs) with models drawn from the MIST (Choi et al. 2016b) stellar isochrones. The SED models (and corresponding predicted photometry) are computed from grids of ATLAS12 model atmospheres (Kurucz 1970) and the spectrum synthesis code SYNTHE (Kurucz 1993). Both atmospheres and SEDs are computed in 1D assuming plane-parallel geometry and LTE. We adopt the solar abundances from Asplund et al. (2009), which is also the abundance scale used in the MIST isochrones. Atomic and molecular line lists are adopted from the latest compilation of R. Kurucz (private communication), and have been astrophysically calibrated against ultra high resolution ($R > 200k$) spectra of the Sun and Arcturus using the same model assumptions as adopted herein (Cargile et al., in prep.). The fit is performed using the nested sampling code *dynesty* (Speagle 2019).

We fit Gl 414A with *MINESweeper* using the available photometry from Gaia DR2 (G/BP/RP), 2MASS (J/H/K_s), and *WISE* (W1/W2/W3). For the Gaia photometry, we assume the filter curves and zero points defined by Maíz Apellániz & Weiler (2018) and photometric corrections published on the mission website².

We find $T_{\text{eff}} = 4239^{+84}_{-83}$, $[\text{Fe}/\text{H}] = +0.25^{+0.04}_{-0.05}$, $R_{\star} = 0.658^{+0.087}_{-0.088}$, $M_{\star} = 0.703^{+0.079}_{-0.080}$, and $L_{\star} = 0.126 \pm 0.012$. These results from are consistent with those we get from *SpecMatch-Emp* and *isoclassify*. Our modeling suggests that Gl 414A has an enhanced alpha-element abundance ($[\alpha/\text{Fe}] \sim +0.6$).

The *MINSWEEPER* analysis gives an age of $2.03^{+3.77}_{-0.57}$ Gyr, which is inconsistent with the *isoclassify* analysis. However, we note that the age of low mass stars is very difficult to determine due to their long lifetimes and slow evolution on the main sequence. A more detailed analysis is needed to establish the age of this system but is beyond the scope of this study.

Due to the high SNR in the spectrum used to perform the spectroscopic analysis (> 350 per resolution element) the formal statistical uncertainties are extremely small. We have seen from ensemble analysis of spectroscopic extraction codes and comparisons with other techniques that the statistical uncertainties from these codes are dwarfed by the systematic uncertainties in the stellar atmosphere and isochrone models in this high SNR regime (e.g., Petigura et al. 2017; Johnson et al. 2017; Pepper et al. 2019). For this reason, we follow the methodology of Petigura et al. (2017) and Johnson et al. (2017) by adding the following terms in quadrature

with our measured *Specmatch-Emp+isoclassify* uncertainties; 100 K for T_{eff} , 0.1 dex for $\log(g)$, and fractional uncertainties of 2% for stellar mass, radius, and luminosity. These additional uncertainty terms were found by comparing the parameters estimated by *Specmatch-Emp+isoclassify* to those from other sources for a large sample of benchmark stars (Yee et al. 2017). In addition, we attempt to incorporate the uncertainty due to our choice of modeling technique by adding the errors from *MINESweeper* in quadrature with those from *SpecMatch-Emp* and *isoclassify*. Our final adopted stellar parameters and associated uncertainties are listed in Table 1.

2.3. Activity Indices

As discussed earlier, Gl 414A is a relatively active K star. We find that the median metrics of stellar activity as measured by the Ca II H&K lines in our Keck/HIRES spectra are $S_{\text{HK}} = 0.98 \pm 0.11$ and $\log R'_{\text{HK}} = -4.72 \pm 0.05$ (Isaacson & Fischer 2010). These values suggest a marginally consistent, but perhaps slightly lower activity level than the values reported in Boro Saikia et al. (2018), who reported $S_{\text{HK}} = 1.14$ and $\log R'_{\text{HK}} = -4.50$. The discrepancy between $\log R'_{\text{HK}}$ from Boro Saikia et al. (2018) and our value is due to differences in the methodology used to convert between S_{HK} and $\log R'_{\text{HK}}$. If we convert their S_{HK} value to $\log R'_{\text{HK}}$ using the methodology of Isaacson & Fischer (2010) we find a value of $\log R'_{\text{HK}} = -4.65$.

3. RADIAL VELOCITY MEASUREMENTS

3.1. Keck/HIRES

We collected 126 RV measurements between UT Jan 14, 1997 and June 16, 2019 using the HIRES instrument on the Keck I telescope (Vogt et al. 1994). This star was observed using the $0''.86 \times 3.5''$ and $0''.86 \times 14''$ slits for a spectral resolution of $R \approx 65,000$ near 5500Å. We extracted RV measurements from each spectrum following the technique described in Marcy & Butler (1992). We observed Gl 414A with a cell of gaseous iodine in the light path just behind the entrance slit. The iodine cell imprints a dense forest of molecular absorption lines onto the stellar spectrum which are used as a simultaneous wavelength and point spread function (PSF) fiducial. We forward modeled each observation in 718 small chunks of spectral width ≈ 2 Å as

$$I_{\text{obs}}(\lambda) = k[T_{I_2}(\lambda) \cdot I_S(\lambda + \Delta\lambda)] \otimes \text{PSF}, \quad (1)$$

where T_{I_2} is the transmission of the iodine cell as measured in a lab, $I_S(\lambda + \Delta\lambda)$ is the intrinsic stellar spectrum

² <https://www.cosmos.esa.int/web/gaia/dr2-known-issues>

Table 1. Stellar Properties of Gl 414A

Parameter	Gl 414A	Source
Alt. names	HD 97101 HIP 54646	Cannon & Pickering (1993) van Leeuwen (2007)
RA	11 11 05.17	Gaia18
Dec	+30 26 45.66	Gaia18
Spectral type	K7V	Gray et al. (2003)
$B - V$ (mag)	1.255	Boro Saikia et al. (2018)
m_V (mag)	8.864 \pm 0.12	Zacharias et al. (2012)
m_G (mag)	7.7281 \pm 0.0007	Gaia18
m_J (mag)	5.764 \pm 0.033	Cutri et al. (2003)
m_H (mag)	5.130 \pm 0.033	Cutri et al. (2003)
m_K (mag)	4.979 \pm 0.033	Cutri et al. (2003)
distance (pc)	11.893 \pm 0.007	Gaia18
T_{eff} (K)	4120 \pm 109	this work (2.1)
$\log(g)$	4.65 \pm 0.04	this work (2.2)
[Fe/H]	0.24 \pm 0.10	this work (2.1)
[α /Fe]	0.58 $^{+0.02}_{-0.08}$	this work (2.2)
R_* (R_{\odot})	0.680 \pm 0.14	this work (2.1)
L_* (L_{\odot})	0.119 \pm 0.013	this work (2.1)
M_* (M_{\odot})	0.650 \pm 0.08	this work (2.1)
Age (Gyr)	12.4 \pm 5.2	this work (2.1)
A_v (mag)	0.02 $^{+0.04}_{-0.01}$	this work (2.2)
Gl 414B		
RA	11 11 02.54	Gaia18
Dec	+30 26 41.32	Gaia18
Spectral type	M2V	Stephenson (1986)
$B - V$ (mag)	2.41 \pm 0.34	Hög et al. (2000); Zacharias et al. (2012)
m_V (mag)	9.983 \pm 0.01	Zacharias et al. (2012)
m_G (mag)	9.0471 \pm 0.0011	Gaia18
m_J (mag)	6.592 \pm 0.019	Cutri et al. (2003)
m_H (mag)	5.975 \pm 0.018	Cutri et al. (2003)
m_K (mag)	5.734 \pm 0.020	Cutri et al. (2003)
distance (pc)	11.877 \pm 0.008	Gaia18
T_{eff} (K)	3663 \pm 70	this work (2.1)
[Fe/H]	0.08 \pm 0.09	this work (2.1)
R_* (R_{\odot})	0.548 \pm 0.017	this work (2.1)
L_* (L_{\odot})	0.048 \pm 0.005	this work (2.1)
M_* (M_{\odot})	0.542 \pm 0.022	this work (2.1)
Age (Gyr)	11.2 \pm 5.9	this work (2.1)

(perturbed by an RV that produces a wavelength shift of $\Delta\lambda$) derived by deconvolving an observed iodine-free stellar spectrum with the instrumental PSF. The product of T_{I_2} and I_S is then convolved with a model of the PSF which is described by a sum of Gaussians and scaled by an arbitrary normalization factor k . We list RVs and Ca II H & K (S_{HK}) activity indices from Keck/HIRES in Table 2.

Table 2. Gl 414A Radial Velocities

BJD _{TDB}	RV	Uncertainty	Instrument ¹	S_{HK}
(- 2440000)	(m s ⁻¹)	(m s ⁻¹)		
10463.01045	-1.39	1.31	k	...
10546.933	-20.30	1.16	k	...
13370.0738	4.00	0.93	j	1.04
13425.06406	-4.16	0.98	j	1.01
16589.03007	-4.77	1.90	a	0.888
16589.03878	-3.88	1.76	a	0.888

(This table is available in its entirety in a machine-readable form in the online journal. A portion is shown here for guidance regarding its form and content.)

¹k = pre-upgrade Keck/HIRES, j = post-upgrade Keck/HIRES, a = APF

3.2. APF/Levy

We collected 351 RV measurements between UT Oct 23, 2013 and June 3, 2019 using the Levy spectrograph on the Automated Planet Finder (APF) telescope (Vogt et al. 2014; Radovan et al. 2014). We used the 1'' \times 3'' slit for a spectral resolution of $R \approx$ 100,000 and reduced the data and extracted velocities in the same way as for Keck/HIRES. RVs and Ca II H & K S_{HK} activity indices from APF/Levy are also listed in Table 2.

3.3. Shane/Hamilton Spectrograph

This star was previously observed by the Twenty-five Year Lick Planet Search (Fischer et al. 2014), with 13 RV measurements collected between UT Jan. 17, 1992 and Feb. 3, 2009 using the Hamilton Spectrograph on the Shane telescope at Lick Observatory. However, the scatter of these measurements is significantly higher than that of the other two datasets and we find that they add very little information to our fits. Including the Lick data would add several more free parameters to the fit, one for each of the CCD upgrades performed on the Hamilton Spectrograph. For this reason, we elect not to include these measurements in our final analysis.

4. VISIBLE-LIGHT PHOTOMETRY

The Kilodegree Extremely Little Telescope (Pepper et al. 2007, KELT) is a small-aperture, wide-field photometric survey searching for transiting planets. The KELT-North telescope is located at Winer Observatory, AZ, and uses an Apogee AP16E detector with 4096 \times 4096 9 μ m pixels and a Mamiya 645 80mm lens. The KELT field of view is 26° \times 26°, with 23'' per pixel, and uses a non-standard wide bandpass comparable to a broad R-band filter.

KELT observed GL 414A in KELT field KN07, obtaining 9516 photometric measurements between UT Dec. 24, 2006 and June 12, 2013. These data were reduced and photometry extracted following the procedures described in Siverd et al. (2012). We used the version of the light curve detrended with the TFA algorithm Kovács et al. (2005). The KELT light curve for GL 414A has an RMS of 7.3mmag and a median absolute deviation of 6.4mmag. With the large KELT pixels, the nearby companion GL 414B is fully blended in the KELT aperture and contributes $\sim 20\%$ to the total flux.

5. DOPPLER ANALYSIS

5.1. Search for Periodic Signals

In order to identify significant periodic signals in the RVs, we used a hierarchical approach that compared a Keplerian model with a given number of planets to one with an additional planet to determine if adding a planet improved the quality of the fit at a statistically significant level. The Keplerian model is of the form:

$$\mathcal{V}_r = \sum_k^{N_{pl}} K_k [\cos(\nu_k + \omega_k) + e_k \cos(\omega_k)] + \gamma_i. \quad (2)$$

where K is the velocity semi-amplitude, e is the eccentricity, ω is the argument of periapsis, and ν is the true anomaly given by $\nu = 2 \tan^{-1} \left(\sqrt{\frac{1+e}{1-e}} \tan \frac{E}{2} \right)$, where E is the eccentric anomaly. γ_i is an offset term used to account for the different mean center-of-mass velocities of each instrument (i).

We created a periodogram by using the Python package `RadVel` (Fulton et al. 2017)³ version 1.2.13 to fit the RV data with a series of circular Keplerian models with fixed orbital periods. We utilized 10,000 search periods evenly spaced in frequency with values ranging between 20 and 6000 days. At each trial period we kept the period and eccentricity fixed while allowing all other orbital parameters to vary. We fit the model using the MAP optimization functionality built into `RadVel`. For fits with two or more planets we kept the orbital parameters of the previously-identified planet(s) fixed to the best-fit values from the $n - 1$ planet version of the model. After completing our search in period space we represented the power at each trial period as the change in the Bayesian Information Criterion (ΔBIC) (Schwarz 1978) with respect to the $n - 1$ planet model.

We began our search by comparing a model with one planet to a constant radial velocity and found that the

signal with the largest ΔBIC was located at 749.16 days. We used this period as our initial guess and fit a new Keplerian orbit where the period and eccentricity were allowed to vary freely. We then incorporated this best-fit model into a new search for a second periodic signal. This revealed another peak at 39.7 days, which we fit with a model in which the parameters of both planets were allowed to vary. We then repeated this same process for two vs. three and three vs. four planets. We continued to iterate until the ΔBIC of the highest peak was less than 10 relative to the noise and found significant periodic signals at 749.16, 39.70, 51.61, and 3063.58 days (Figure 1).

5.2. Stellar Activity

In order to determine whether or not any of the signals were related to stellar activity, we analyzed 6 years of photometric data from KELT. We used these data to create a Lomb-Scargle periodogram (Figure 2), which had a peak at a period of 42 days. We estimated the season-to-season variance in this period by splitting the data into individual observing seasons and identifying the highest peak for each season. We found that this variance was approximately 4 days. We found an equivalent peak at 40 days in the S_{HK} measurements of the star from APF (Figure 4). We therefore concluded that the 39.7 day signal in our RV periodograms was most likely a stellar activity signal related to the star's rotation period.

The S_{HK} periodogram from Keck had an additional strong peak at a period of 2976 days, which was similar to the RV periodogram peak at 3063 days in our four-planet model. We concluded that this signal was most likely related to the magnetic activity cycle of the star, which is typically on the order of a decade for FGK stars (Lovis et al. 2011).

5.3. Orbital Characterization

We used the affine-invariant Markov Chain Monte Carlo (MCMC) sampler `emcee` (Foreman-Mackey et al. 2013) to determine the final posterior probability distribution for our two-planet model. This functionality is available as a built-in feature of `RadVel`. We accounted for the approximately 39 day stellar activity signal using a Gaussian process (GP) model with a quasi-periodic kernel following a process similar to that described in Kosiarek et al. (2018). We chose not to include the 3063 day signal in this analysis because including it in the model does not significantly change the BIC. The elements of the covariance kernel are of the form:

³ radvel.readthedocs.io

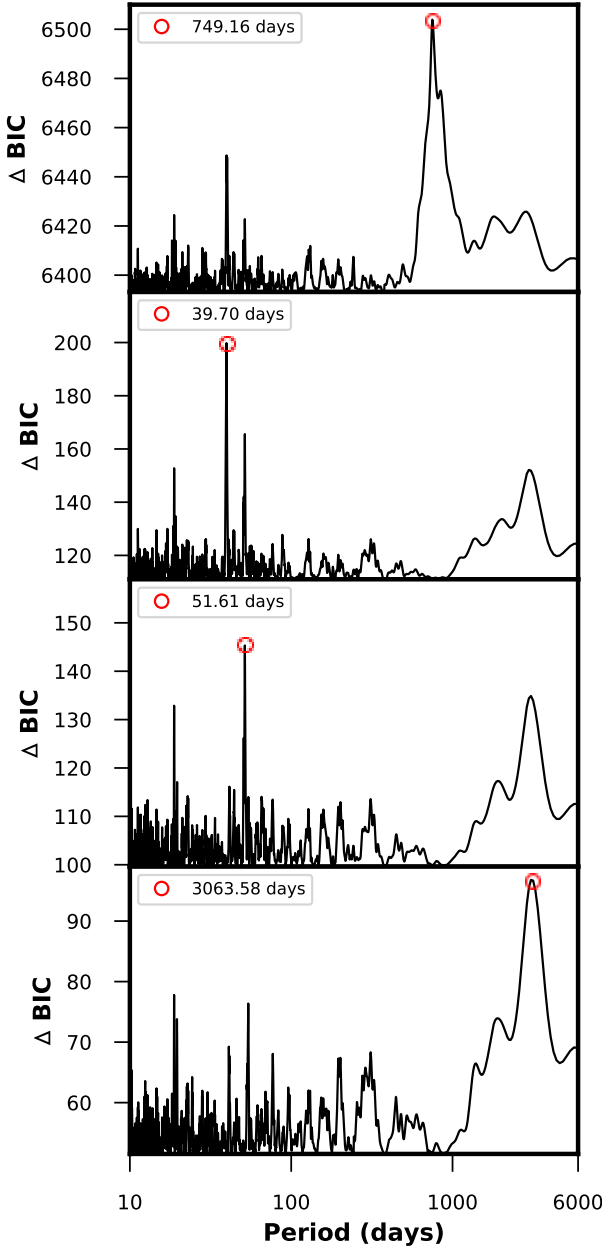


Figure 1. Results of the first four iterations of the multi-planet periodogram search described in Section 5.1. Shown here are the peaks at about 750, 40, 51, and 3000 days. Each panel has the previous highest-signal subtracted out to look for subsequent signals.

$$C_{ij} = \eta_1^2 \exp \left[-\frac{|t_i - t_j|^2}{\eta_2^2} - \frac{\sin^2 \left(\frac{\pi |t_i - t_j|}{\eta_3} \right)}{2\eta_4^2} \right] \quad (3)$$

where the hyper-parameter η_1 is the amplitude, η_2 is the exponential decay timescale, η_3 is the period, and η_4 is the characteristic length of the periodic component.

The Keplerian and GP likelihoods are given by:

$$\ln \mathcal{L}_i = -\frac{1}{2} \sum_j \frac{(\mathcal{V}_{r,j} - d_j)^2}{e_j^2 + \sigma_i^2} - \ln \sqrt{2\pi(e_j^2 + \sigma_i^2)} \quad (4)$$

$$\ln \mathcal{L}_{gp} = \frac{1}{2} (r^T C^{-1} r - \ln[\det(C)] - N \ln(2\pi)). \quad (5)$$

respectively, where \mathcal{V}_r is the Keplerian model (Equation 2), e_j is the error associated with each data point d_j , σ_i is the jitter term for each instrument, r is the vector of residuals, C is the covariance matrix, and N is the number of measurements.

The total log-likelihood of all components of the model is then:

$$\ln \mathcal{L} = \sum_i \ln \mathcal{L}_i + \ln \mathcal{L}_{gp}. \quad (6)$$

We first trained the GP on the photometric data to extract posteriors for the exponential decay length (η_2) and GP period (η_3). We then repeated this training on the S_{HK} values using the posteriors from the photometric fit as priors. The priors are applied numerically using a kernel density estimator to approximate the shapes of the posteriors. The resulting posteriors on η_2 and GP period η_3 are then included as priors in the full RV fit. After training on both the photometric and S_{HK} data sets, we found that $\eta_2 = 31.08^{+8.45}_{-9.43}$ days and $\eta_3 = 40.11^{+6.34}_{-4.00}$ days. We allowed η_1 to vary independently in each fit because the activity-driven amplitudes of the photometry, S_{HK} values, and RVs are unrelated. We fixed the value of η_4 at 0.5, because allowing it to vary would cause unphysical effects in the fit, as shown in López-Morales et al. (2016). The GP fit to the photometric data in Figure 3 indicates that the 40 day signal is not strictly periodic, as expected for stellar activity. We show the RV data and corresponding best-fit model in Figure 5.

6. DISCUSSION

We find compelling evidence for two planets in this system with orbital periods of 750 days and 51 days and minimum masses of $60.3 M_{\oplus}$ and $9.9 M_{\oplus}$, respectively. We attribute the 40 day signal in the RV data to rotationally-modulated starspots, and the 3000 day signal to the magnetic activity cycle of the star.

We used the Python code **Forecaster**, which is based on the probabilistic mass-radius relationship in Chen & Kipping (2017), to estimate radii corresponding to our minimum mass measurements. We predict that if its orbit is viewed close to edge-on, planet b should have a radius of $R_b = 3.0 R_{\oplus}$ and planet c should have a

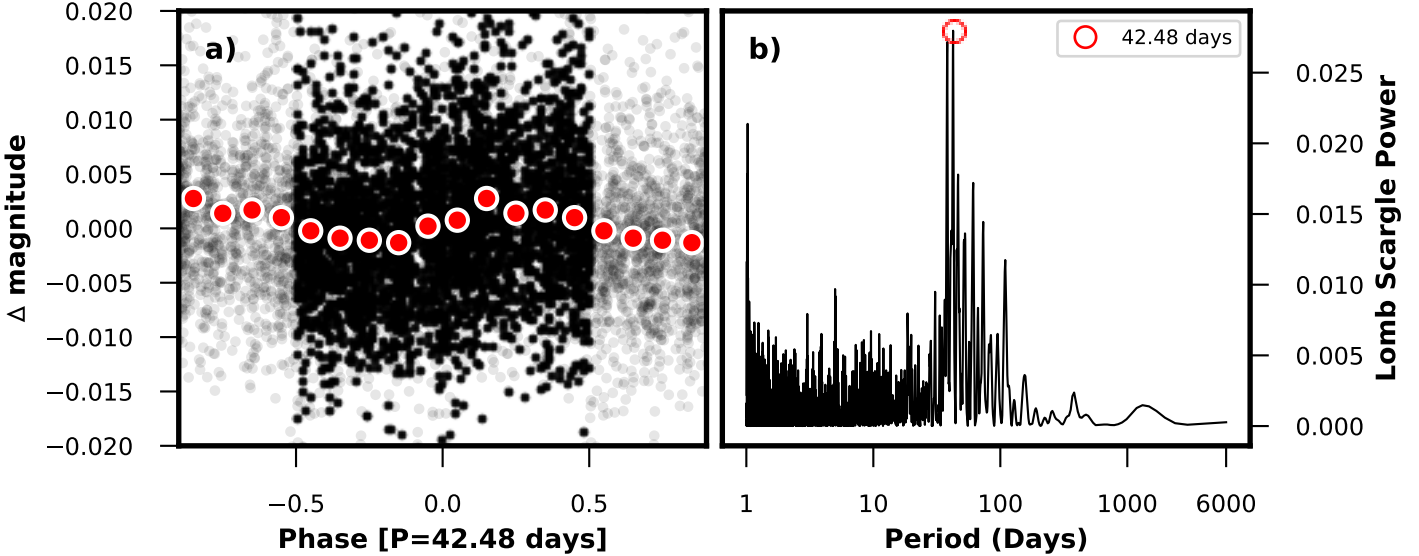


Figure 2. *Left:* KELT photometry phase-folded at a period of 42.48 days. The red dots show the values binned at intervals of 0.1 units of phase. *Right:* Lomb-Scargle periodogram of the KELT photometry.

radius of $R_c = 8.9 R_{\oplus}$. Assuming the bond albedo of planet b is equal to the mean total albedo of super-Earths ($A_t = 0.32$, Demory 2014) and planet c is equal to that of Saturn ($A_t = 0.343$, Mallama et al. 2017), we calculate predicted equilibrium temperatures of $T_{eq,b} = 303.7 \pm 32.5$ K and $T_{eq,c} = 123.3 \pm 13.2$ K for these two planets. We list the full set of derived properties for each planet in Table 3.

6.1. Orbital Dynamics

We simulated the system using the REBOUND N-body integration code (Rein & Liu 2012; Rein & Tamayo 2015) to check for stability and investigate the orbital dynamics. We initially assumed that the orbits are coplanar and set the orbital elements to their MAP values. We simulated the system in this configuration for 10 million years with a time step of 0.17 days. The system remained stable in this configuration throughout the simulation. Figure 6 shows the evolution of eccentricity and the argument of periastron (ω) as a function of time for the first 50 thousand years of the simulation. ω_b precesses at a relatively rapid rate of 360 degrees every ~ 2500 years. The eccentricities of both planets trade off with each other on this same timescale. ω_c precesses more slowly, with a period of ~ 25000 years, but the rate of precession oscillates at the shorter timescale (~ 2500 years). To test the sensitivity of these precession rates to the initial conditions we also draw 10 sets of orbital parameters from the posterior distributions as starting points for a suite of N-body simulations. We find that the precession timescales vary by $\sim 30\%$, but the general properties of the orbital evolution remain constant.

Table 3. Planet Parameters

Parameter	Value	Units
P_b	$50.817^{+0.031}_{-0.03}$	days
T_{conj_b}	$2454203.2^{+1.9}_{-2.4}$	days
e_b	$0.48^{+0.12}_{-0.16}$	
ω_b	$2.32^{+0.42}_{-0.59}$	radians
K_b	$2.5^{+0.58}_{-0.65}$	m s^{-1}
$e_b \sin \omega_b$	$0.44^{+0.19}_{-0.26}$	
$e_b \cos \omega_b$	$-0.46^{+0.28}_{-0.20}$	
a_b	0.240 ± 0.01	AU
$M_b \sin i$	$8.78^{+3.10}_{-2.47}$	M_{\oplus}
R_b	$2.95^{+1.11}_{-0.91}$	R_{\oplus}
$T_{eq,b}$	303.7 ± 32.5	K
P_c	$748.3^{+1.3}_{-1.2}$	days
T_{conj_c}	$2454205.0^{+5.0}_{-5.4}$	days
e_c	$0.093^{+0.1}_{-0.064}$	
ω_c	$1.6^{+0.74}_{-2.8}$	radians
K_c	$5.45^{+0.77}_{-0.75}$	m s^{-1}
$e_c \sin \omega_c$	$0.21^{+0.18}_{-0.16}$	
$e_c \cos \omega_c$	$-0.07^{+0.19}_{-0.26}$	
a_c	1.43 ± 0.06	AU
$M_c \sin i$	$56.27^{+10.43}_{-9.91}$	M_{\oplus}
R_c	$8.78^{+4.03}_{-2.66}$	R_{\oplus}
$T_{eq,c}$	123.3 ± 13.2	K

We measure a significant eccentricity for the inner planet ($e_b = 0.48^{+0.12}_{-0.16}$) while the outer, more massive planet, is on a nearly circular orbit. The relatively large

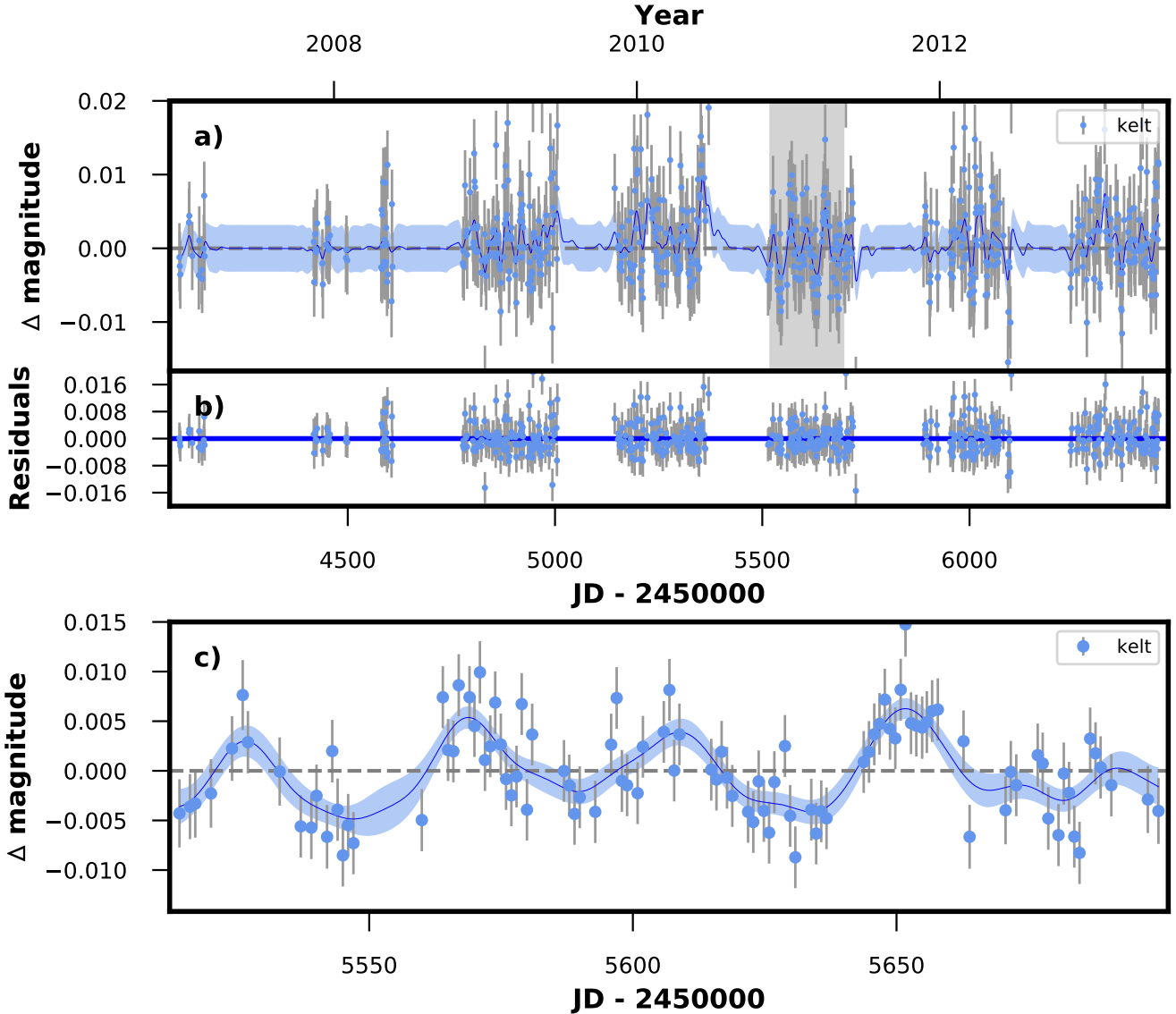


Figure 3. a) Photometric data from KELT (blue filled circles). The blue line shows the best fit Gaussian process model, with uncertainties shown as light blue bands. The grey highlighted section is displayed in more detail in panel c. b) Fit residuals c) A zoomed in view of a single season of photometric data where the quasi-periodic modulations are clearly visible.

eccentricity of the inner planet in this system might plausibly be due to some kind of past dynamical instability (Huang et al. 2017, Carrera et al. 2019). If the two planets have a mutual inclination greater than $\sim 45^\circ$, the inner planet could also be due to Kozai-Lidov oscillations where it cycles between states with high inclination and high eccentricity (Kiseleva et al. 1998). However, for planets close to their host stars general-relativistic (GR) precession may also be significant and can dampen the amplitude of the Kozai-Lidov oscillations (e.g., Ford et al. 2000; Fabrycky & Tremaine 2007). Following the methodology of Yee et al. (2018) we calculate the GR and Kozai timescales for planet b. We find

that the GR timescale is $\tau_{\text{GR}} \sim 5$ Myrs and the Kozai timescale is $\tau_{\text{Kozai}} \sim 24$ kyrs. Since $\tau_{\text{Kozai}} \ll \tau_{\text{GR}}$ it is possible that this system is currently undergoing Kozai oscillations.

We explored the impact of mutual inclination on the system architecture by running many REBOUND simulations, each time perturbing the inclination and initial eccentricity of the inner planet keeping the other orbital elements fixed to their MAP values. For each simulation we recorded the maximum eccentricity reached by the inner planet during the 50 thousand year simulation (Figure 7). We find that if the orbit of the inner planet was initially circular, the mutual inclination of the sys-

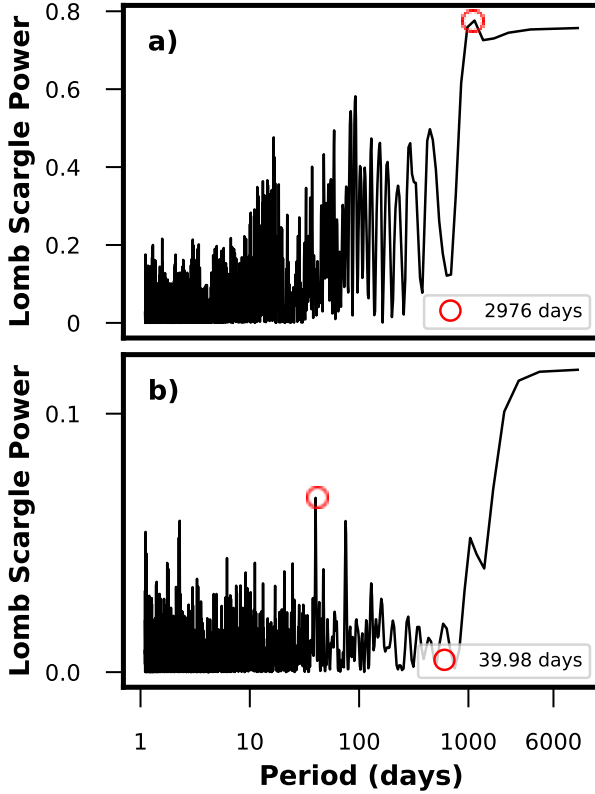


Figure 4. a) LS periodogram of the S_{HK} values from Keck-HIRES. The peak seen here is related to the magnetic activity cycle of the star. b) LS periodogram of S_{HK} values from APF/Levy. This signal is similar to the one we see at 39.6 days in the RVs and 42.5 days in the photometry.

tem must be $\gtrsim 45$ degrees in order to explain the planet b's current eccentricity.

For planets that come close to the star during periastron, tidal circularization is expected to damp out the eccentricity induced by Kozai oscillations or other dynamical interactions (e.g., Fabrycky & Tremaine 2007). We estimated the tidal circularization timescales for this system using the method outlined in Albrecht et al. (2012). Planets b and c both have extremely long tidal circularization times, at 3.2×10^{11} Gyr and 3.8×10^{14} Gyr respectively. We therefore expect that any dynamically-induced orbital eccentricity should persist to the present day.

6.2. Transit Search

We calculate a priori transit probabilities of 1% and 0.2% for planets b and c, respectively. The a posteriori transit probabilities are likely slightly higher (Stevens & Gaudi 2013), but it is unlikely that either of them transits. If they were to transit, we can use the radius estimates from the previous section to calculate predicted transit depths of 0.16% for planet b and 1.4% for planet

c after accounting for 20% dilution in the KELT photometry due to Gl 414B. We plot the KELT photometry phase-folded on the ephemeris of each planet in Figure 8. We note that there appears to be what looks like a transit signal in both phase-folded light curves, but that the phase of these two signals is inconsistent with the predicted time of conjunction for each of the two planets. Upon closer inspection, both signals also occur adjacent to a gap in the data, where instrumental and telluric variations are more likely to create a false positive. We therefore conclude that there is no evidence to suggest that either planet is transiting.

6.3. Direct Imaging Prospects

At a distance of just 12 pc, this relatively cool star is a promising prospect for direct imaging studies. We find that the planets in this system have projected separations of 20 and 120 mas. We compare these separations to the inner working angle (IWA) of two ground-based direct imaging instruments. The Keck Planet Imager and Characterizer (KPIC) (Mawet et al. 2018) has an IWA of 40-100 mas, and Spectro-Polarimetric High contrast imager for Exoplanets REsearch (SPHERE) (Beuzit et al. 2019) has an IWA of 50-80 mas. We also compare these angles to the IWA of two of the coronagraphs on the James Webb Space Telescope (JWST) (Gardner et al. 2006). On the Near-Infrared Camera (NIRCam), the IWA of the largest circular coronagraph is 80 mas, and on the Mid-Infrared Instrument (MIRI) the IWA of the 4QPM1 coronagraph is 33 mas. Planet c is outside the IWA of all of these instruments.

We calculate the contrast of planet c in the K band, as well as in the wavelength bands of the NIRCam F444W Filter ($4.4 \mu\text{m}$) and the MIRI F1065C filter ($10.6 \mu\text{m}$). In the K band, the contrast would be 2.5×10^{-11} , which rules out ground-based instruments that operate in the near-infrared, like KPIC and SPHERE. At the wavelength of the NIRCam F444W filter the contrast of planet c with respect to its host star is 3.5×10^{-7} . At the wavelength of the MIRI F1065C filter planet c has a contrast of 6.3×10^{-6} . Neither of these contrasts are large enough to make Gl 414A c visible with JWST (Beichman et al. (2010), Boccaletti et al. (2015)). However, this planet may be a candidate in the future for imaging with a Mid-Infrared Adaptive Optics system on the Thirty Meter Telescope (Chun et al. 2006).

6.4. Habitability

Using the model described in Kopparapu et al. (2013), we calculate that the habitable zone around this star should lie between 0.37 and 0.70 AU. The planet c falls well outside this zone, but planet b is just inside this

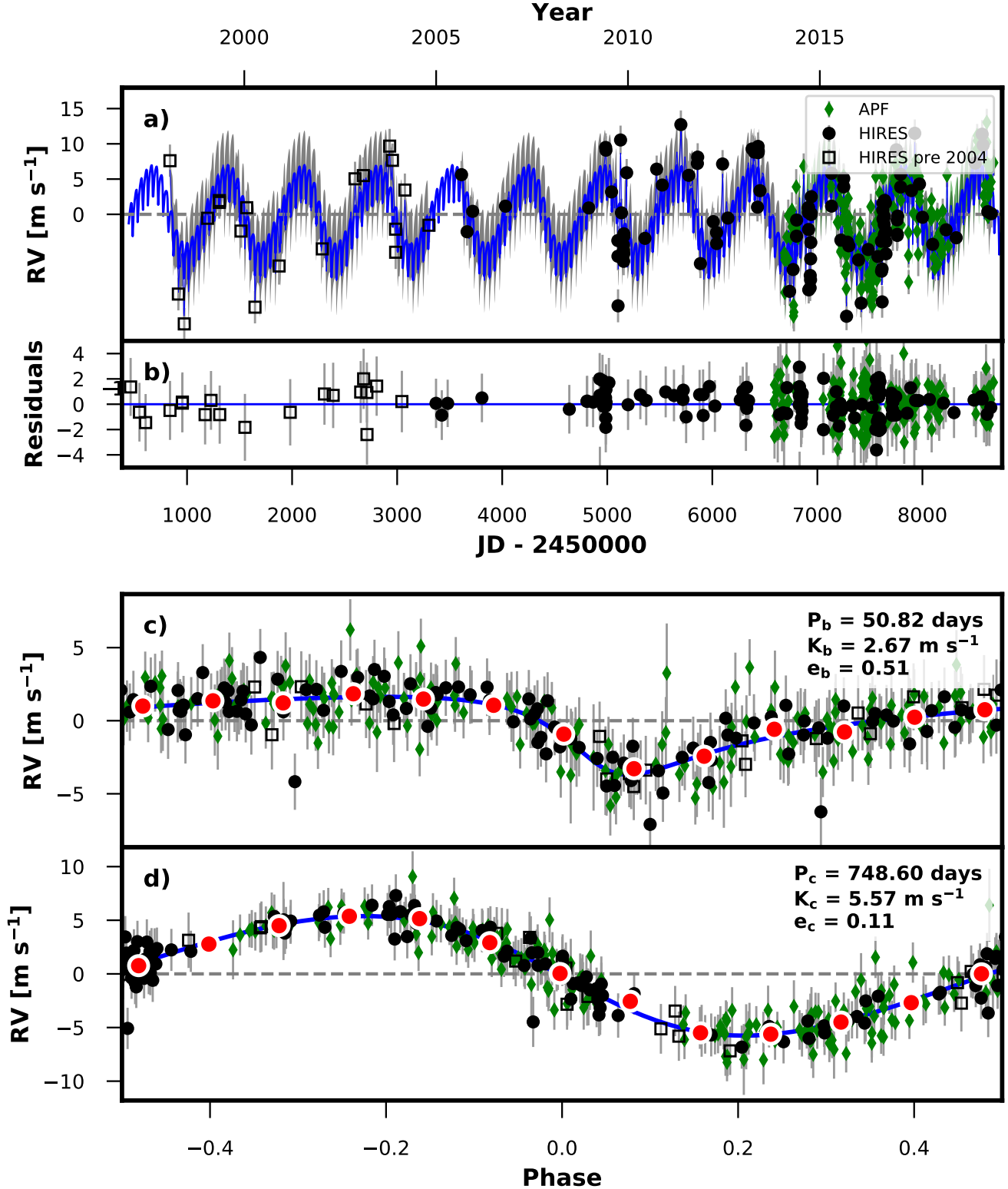


Figure 5. a) RV timeseries with the best fit two-planet model and Gaussian process stellar activity model overplotted in blue. The GP uncertainty is shown as grey bands. b) Fit residuals. c) RVs phase-folded to the ephemeris of planet b, with the Keplerian signal of planet c subtracted. Binned data is shown as red dots and the phase-folded model is shown as a blue line. d) RVs phase-folded to the ephemeris of planet c, with the Keplerian signal of planet b subtracted. Binned data are shown as red dots and the phase-folded model is plotted as a blue line.

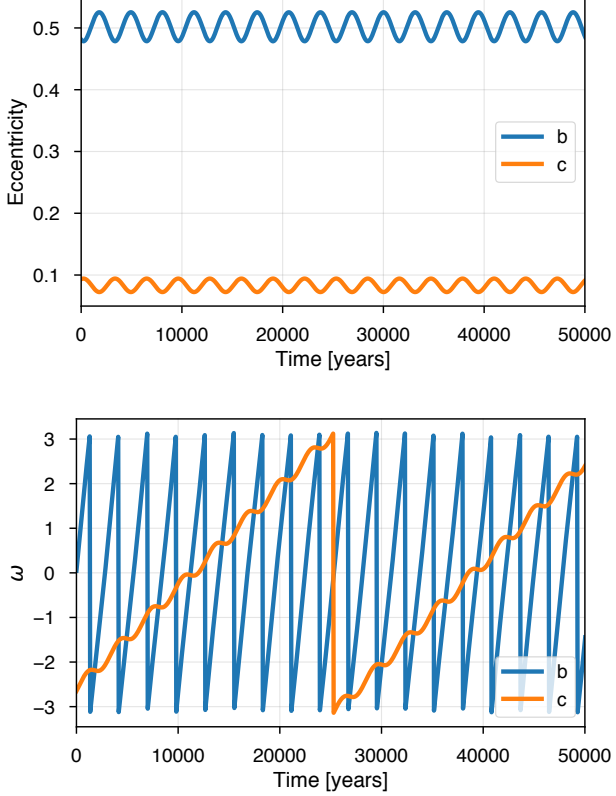


Figure 6. Evolution of orbital parameters from a N-body simulation assuming coplanar orbits. *Top*: Eccentricity as a function of time for each planet. *Bottom*: Argument of periastron (ω) for each planet as a function of time. Each planet’s eccentricity oscillates slightly as ω_b precesses with a timescale of ≈ 2.5 kyr. ω_c precesses more slowly, with a timescale of ≈ 25 kyr.

inner edge. If we use the more optimistic model from Zsom et al. (2013), the inner edge of the habitable zone may be as close as 0.21 AU. With a semi-major axis of 0.24 AU, planet b would fall within this habitable zone range. However, planet b has a minimum mass of $8.8 M_{\oplus}$ which likely corresponds to a substantial volatile-rich envelope (Weiss & Marcy 2014), so it is not a good candidate for habitability.

7. SUMMARY & CONCLUSION

We present the discovery of a sub-Neptune planet and a sub-Saturn planet orbiting the bright K7 dwarf Gl 414A. The minimum masses of the planets are $M_b \sin i_b = 8.78_{-2.47}^{+3.10} M_{\oplus}$ and $M_c \sin i_b = 56.27_{-9.91}^{+10.43} M_{\oplus}$ and they orbit with semi-major axes $a_b = 0.240 \pm 0.01$ AU and $a_c = 1.43 \pm 0.06$ AU. Planet c resides near the inner edge of the star’s habitable zone, but its minimum mass is large enough that it likely possesses a substantial volatile-rich envelope. Figure 9 shows the

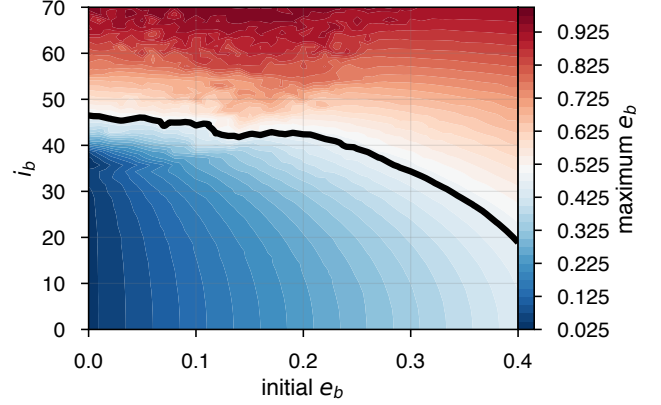


Figure 7. Grid of N-body simulations. Each simulation starts with a different initial eccentricity and inclination for the inner planet. The color-scale shows the maximum eccentricity reached by the inner planet during each 50 kyr simulation. The thick black lines shows the minimum combination of initial eccentricity and mutual inclination needed to explain the current eccentricity of planet b.

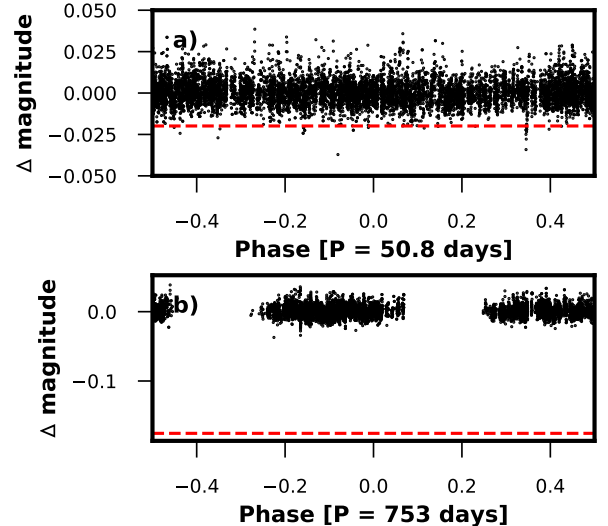


Figure 8. KELT photometry phase-folded on the ephemeris of planet b (top) and planet c (bottom). The dotted red line shows the predicted transit depth. We see no transit signals at these depths and locations

period vs. mass of all currently known planets detected using the radial velocity technique and places Gl 414A b and Gl 414A c in context.

In a search of the 4201 confirmed planets listed in the NASA Exoplanet Archive, we found eight other planets in multi-planet systems where one of the planets had an orbital period between 30 and 100 days and an eccentricity greater than 0.4. (HD 163607, Kepler-419,

HD 168443, HD 37605, Kepler-432, HD 74156, V1298 Tau, and HD 147018.)⁴ In seven of these systems, there are exactly two planets detected. The high eccentricity planet is always the inner planet, and the outer planet always has a large separation from the inner planet ($P > 400$ days). This suggests that this class of planets may have a common dynamical origin; for example, it is possible that these system architectures all arose from Kozai-Lidov oscillations. These systems may represent a dynamically active subset of the larger exoplanet population.

Simulations in this paper made use of the REBOUND code which is freely available at <http://github.com/hannorein/rebound>.

Facility: Automated Planet Finder (Levy), Keck:I (HIRES), Exoplanet Archive

ACKNOWLEDGMENTS

We are grateful to the time assignment committees of the California Institute of Technology, the University of California, the University of Hawaii, and NASA for their generous allocations of observing time. Without their long-term commitment to RV monitoring, these planets would likely remain unknown. We gratefully acknowledge the efforts and dedication of the staffs of the W. M. Keck Observatory and Mt. Hamilton. Research at the Lick Observatory is partially supported by a generous gift from Google. We thank Geoff Marcy and Debra Fischer for their many nights of observing that contributed to the Keck data presented in this work, and R. Paul Butler and S. S. Vogt for many years of contributing to the data presented here. AWH acknowledges NSF grant AST-1517655. MRK acknowledges support from the NSF Graduate Research Fellowship, grant No. DGE 1339067. DJS was supported as an Eberly Research Fellow by the Eberly College of Science at the Pennsylvania State University.

The authors extend special thanks to those of Hawaiian ancestry on whose sacred mountain of Maunakea we are privileged to be guests. Without their generous hospitality, the Keck observations presented herein would not have been possible.

This work made use of the GNU Parallel package for large-scale multiprocessing (Tange 2018). This research has made use of the NASA Exoplanet Archive, which is operated by the California Institute of Technology, under contract with the National Aeronautics and Space Administration under the Exoplanet Exploration Program. This work made extensive use of the `scipy` (Virtanen et al. 2019), `numpy` (van der Walt et al. 2011), `matplotlib` (Hunter 2007), and `pandas` (McKinney 2010) Python packages.

⁴ <https://exoplanetarchive.ipac.caltech.edu/>

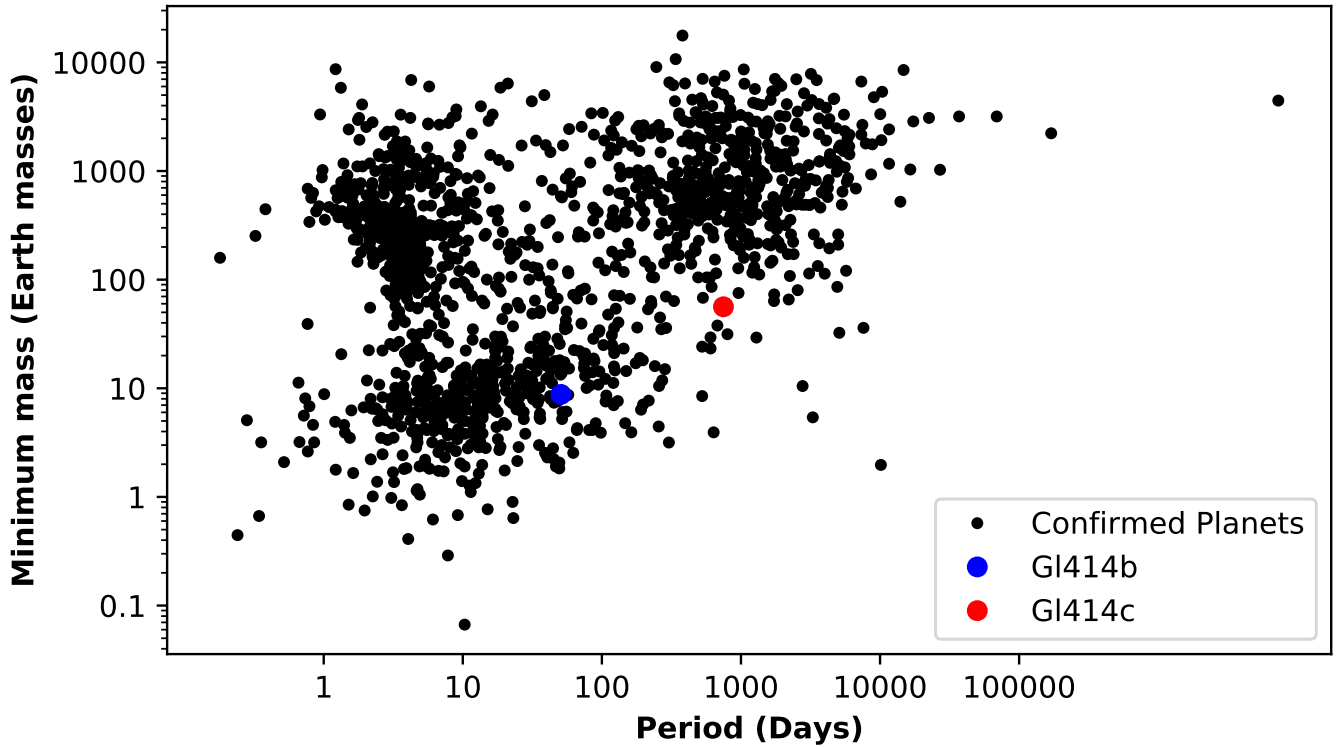


Figure 9. Plot of $M \sin i$ vs. orbital period for all known exoplanets as of 8/28/2020 with measured masses, with Gl 414A b and Gl 414A c placed in context. This plot illustrates that these two planets are among the longest period planets that have been detected to date in their respective mass ranges.

REFERENCES

Albrecht, S., Winn, J. N., Johnson, J. A., et al. 2012, *The Astrophysical Journal*, 757, 18

Asplund, M., Grevesse, N., Sauval, A. J., & Scott, P. 2009, *ARA&A*, 47, 481

Bastien, F. A., Stassun, K. G., Basri, G., & Pepper, J. 2013, *Nature*, 500, 427

Beichman, C. A., Krist, J., Trauger, J. T., et al. 2010, *PASP*, 122, 162

Berger, T. A., Huber, D., van Saders, J. L., et al. 2020, *AJ*, 159, 280

Beuzit, J. L., Vigan, A., Mouillet, D., et al. 2019, arXiv e-prints, arXiv:1902.04080

Boccaletti, A., Lagage, P.-O., Baudoz, P., et al. 2015, *Publications of the Astronomical Society of the Pacific*, 127, 633

Boro Saikia, S., Marvin, C. J., Jeffers, S. V., et al. 2018, *A&A*, 616, A108

Cannon, A. J., & Pickering, E. C. 1993, *VizieR Online Data Catalog*, III/135A

Cargile, P. A., Conroy, C., Johnson, B. D., et al. 2019, arXiv e-prints, arXiv:1907.07690

Chen, J., & Kipping, D. 2017, *ApJ*, 834, 17

Choi, J., Dotter, A., Conroy, C., et al. 2016a, *ApJ*, 823, 102

—. 2016b, *ApJ*, 823, 102

Chun, M. R., Elias, J., Ellerbroek, B., et al. 2006, in *Advances in Adaptive Optics II*, ed. B. L. Ellerbroek & D. B. Calia, Vol. 6272, International Society for Optics and Photonics (SPIE), 252 – 261

Cutri, R. M., Skrutskie, M. F., van Dyk, S., et al. 2003, *VizieR Online Data Catalog*, 2246, 0

Dai, F., Winn, J. N., Gandolfi, D., et al. 2017, *AJ*, 154, 226

Demory, B.-O. 2014, *The Astrophysical Journal*, 789, L20

Dotter, A. 2016, *ApJS*, 222, 8

Fabrycky, D., & Tremaine, S. 2007, *ApJ*, 669, 1298

Fischer, D. A., Marcy, G. W., & Spronck, J. F. P. 2014, *ApJS*, 210, 5

Ford, E. B., Kozinsky, B., & Rasio, F. A. 2000, *ApJ*, 535, 385

Foreman-Mackey, D., Hogg, D. W., Lang, D., & Goodman, J. 2013, *PASP*, 125, 306

Fulton, B. J. 2017, PhD thesis, University of Hawai'i at Manoa

Fulton, B. J., & Petigura, E. A. 2018, *AJ*, 156, 264

Fulton, B. J., Howard, A. W., Weiss, L. M., et al. 2016, *ApJ*, 830, 46

Fulton, B. J., Petigura, E. A., Howard, A. W., et al. 2017, *AJ*, 154, 109

Gaia Collaboration, Brown, A. G. A., Vallenari, A., et al. 2018, ArXiv e-prints, arXiv:1804.09365

Gardner, J. P., Mather, J. C., Clampin, M., et al. 2006, *Space Science Reviews*, 123, 485606

Gray, R. O., Corbally, C. J., Garrison, R. F., McFadden, M. T., & Robinson, P. E. 2003, *AJ*, 126, 2048

Høg, E., Fabricius, C., Makarov, V. V., et al. 2000, *A&A*, 355, L27

Howard, A. W., Johnson, J. A., Marcy, G. W., et al. 2009, *ApJ*, 696, 75

Howard, A. W., Marcy, G. W., Johnson, J. A., et al. 2010, *Science*, 330, 653

Huber, D., Zinn, J., Bojsen-Hansen, M., et al. 2017, *ApJ*, 844, 102

Hunter, J. D. 2007, *Computing in Science & Engineering*, 9, 90

Isaacson, H., & Fischer, D. 2010, *The Astrophysical Journal*, 725, 875

Johnson, J. A., Petigura, E. A., Fulton, B. J., et al. 2017, ArXiv e-prints, arXiv:1703.10402

Kiseleva, L. G., Eggleton, P. P., & Mikkola, S. 1998, *MNRAS*, 300, 292

Kopparapu, R. K., Ramirez, R., Kasting, J. F., et al. 2013, *The Astrophysical Journal*, 765, 131

Kosiarek, M. R., Crossfield, I. J. M., Hardegree-Ullman, K. K., et al. 2018, ArXiv e-prints, arXiv:1812.08241

Kovács, G., Bakos, G., & Noyes, R. W. 2005, *MNRAS*, 356, 557

Kurucz, R. L. 1970, *SAO Special Report*, 309

—. 1993, SYNTHE spectrum synthesis programs and line data (SYNTHE Spectrum Synthesis Programs and Line Data. Kurucz CD-ROM No. 18. Cambridge)

López-Morales, M., Haywood, R. D., Coughlin, J. L., et al. 2016, *The Astronomical Journal*, 152, 204

Lovis, C., Dumusque, X., Santos, N. C., et al. 2011, ArXiv e-prints, arXiv:1107.5325

Maíz Apellániz, J., & Weiler, M. 2018, *A&A*, 619, A180

Mallama, A., Krobusek, B., & Pavlov, H. 2017, *Icarus*, 282, 19

Mann, A. W., Dupuy, T., Kraus, A. L., et al. 2019, *ApJ*, 871, 63

Marcy, G. W., & Butler, R. P. 1992, *PASP*, 104, 270

Mason, B. D., Wycoff, G. L., Hartkopf, W. I., Douglass, G. G., & Worley, C. E. 2001, *AJ*, 122, 3466

Mawet, D., Bond, C. Z., Delorme, J. R., et al. 2018, in *Society of Photo-Optical Instrumentation Engineers (SPIE) Conference Series*, Vol. 10703, Proc. SPIE, 1070306

McKinney, W. 2010, in *Proceedings of the 9th Python in Science Conference*, ed. S. van der Walt & J. Millman, 51 – 56

Pepper, J., Pogge, R. W., DePoy, D. L., et al. 2007, *PASP*, 119, 923

Pepper, J., Kane, S. R., Rodriguez, J. E., et al. 2019, ArXiv e-prints, arXiv:1911.05150

Petigura, E. A., Howard, A. W., Marcy, G. W., et al. 2017, *AJ*, 154, 107

Radovan, M. V., Lanclos, K., Holden, B. P., et al. 2014, in *Society of Photo-Optical Instrumentation Engineers (SPIE) Conference Series*, Vol. 9145, *Society of Photo-Optical Instrumentation Engineers (SPIE) Conference Series*, 2

Rein, H., & Liu, S. F. 2012, *A&A*, 537, A128

Rein, H., & Tamayo, D. 2015, *MNRAS*, 452, 376

Schwarz, G. 1978, *Ann. Statist.*, 6, 461

Siverd, R. J., Beatty, T. G., Pepper, J., et al. 2012, *ApJ*, 761, 123

Speagle, J. S. 2019, ArXiv e-prints, arXiv:1904.02180

Stephenson, C. B. 1986, *AJ*, 92, 139

Stevens, D. J., & Gaudi, B. S. 2013, *PASP*, 125, 933

Tange, O. 2018, *GNU Parallel 2018 (Ole Tange)*, doi:10.5281/zenodo.1146014

van der Walt, S., Colbert, S. C., & Varoquaux, G. 2011, *Computing in Science Engineering*, 13, 22

van Leeuwen, F. 2007, *A&A*, 474, 653

Virtanen, P., Gommers, R., Oliphant, T. E., et al. 2019, ArXiv e-prints, arXiv:1907.10121

Vogt, S. S., Allen, S. L., Bigelow, B. C., et al. 1994, in *Proc. SPIE Instrumentation in Astronomy VIII*, David L. Crawford; Eric R. Craine; Eds., 2198, 362

Vogt, S. S., Radovan, M., Kibrick, R., et al. 2014, *PASP*, 126, 359

Weiss, L. M., & Marcy, G. W. 2014, *ApJ*, 783, L6

Yee, S. W., Petigura, E. A., & von Braun, K. 2017, *ApJ*, 836, 77

Yee, S. W., Petigura, E. A., Fulton, B. J., et al. 2018, *AJ*, 155, 255

Zacharias, N., Finch, C. T., Girard, T. M., et al. 2012, *VizieR Online Data Catalog*, I/322A

Zsom, A., Seager, S., de Wit, J., & Stamenković, V. 2013, *ApJ*, 778, 109